Nanoscale

PAPER

View Article Online
View Journal | View Issue

Cite this: *Nanoscale*, 2023, **15**, 5726

Light-powered swarming phoretic antimony chalcogenide-based microrobots with "on-the-fly" photodegradation abilities†

Anna Jancik-Prochazkova [a] and Martin Pumera *[a,b,c,d]

Microrobots are at the forefront of research for biomedical and environmental applications. Whereas a single microrobot exhibits quite low performance in the large-scale environment, swarms of microrobots are representing a powerful tool in biomedical and environmental applications. Here, we fabricated phoretic Sb_2S_3-based microrobots that exhibited swarming behavior under light illumination without any addition of chemical fuel. The microrobots were prepared in an environmentally friendly way by reacting the precursors with bio-originated templates in aqueous solution in a microwave reactor. The crystalline Sb_2S_3 material provided the microrobots with interesting optical and semiconductive properties. Because of the formation of reactive oxygen species (ROS) upon light illumination, the microrobots possessed photocatalytic properties. To demonstrate the photocatalytic abilities, industrially used dyes, quinoline yellow and tartrazine were degraded using microrobots in the "on-the-fly" mode. Overall, this proof-of-concept work showed that Sb_2S_3 photoactive material is suitable for designing swarming microrobots for environmental remediation applications.

Received 7th January 2023,
Accepted 26th February 2023

DOI: 10.1039/d3nr00098b

rsc.li/nanoscale

Introduction

Microrobots are autonomous micro-scaled devices that are designed to accomplish a specific mission on microscale.[1–3] Microrobots are chemically programmed to collect, transport, and deliver cargo,[4–6] degrade pollutants[7,8] and bacterial contamination,[9,10] or sense desired substances,[11,12] *etc*. However, a single microrobot exhibits relatively poor efficiency when studied in the macro-scale. Inspired by morphogenesis in biology, microrobotic systems were programmed to communicate and cooperate with each other by forming swarms of microrobots.[13,14] The swarming microrobots promise a powerful tool for medical and environmental applications, as they can react in response to environmental stimuli, such as change in morphology, cargo loading and transport, imaging, *etc*.[15–17] Swarming behavior can be induced by using various external stimuli, *i.e.* magnetic field, light, acoustic or electric field.[18] Light-induced swarm formation is quite a versatile approach considering its low-cost instrumentation, precise control, and biocompatibility. The mechanism of light-induced swarming lies in different mechanisms, such as electrophoresis, diffusiophoresis, and thermophoresis.[19] A typical example of light-induced swarm formation are TiO_2-based swarming photophoretic microrobots.[20] Upon light irradiation, TiO_2 microrobots show schooling behavior consisting of the expansion and contraction of the swarms that act as a microfirework or micropump system due to photophoretic properties.[21] Eventually, due to negative phototaxis, the swarms can move within the sample and transport desired substances.[22] L. Wang *et al.*[23] used phoretic interactions among TiO_2-based microrobots to remove microplastics from aqueous samples. In addition to TiO_2, light-induced swarming behavior was observed in various types of semiconductors, for example organic photoactive molecules[24] and polymers,[25] silver chloride,[26] silver phosphate,[27] iron oxide,[28] or chalcogenide semiconductors.[29,30] The latter is also known for good thermodynamic stability, facile synthesizability and dopability, and unique optoelectrical properties that enable their application in solar cells, thin film transistors, diodes, or water splitting photoelectrocatalysts.[31] Recently, chalcogenide semiconductors have been applied as suitable materials for the fabrication of light-driven microrobots; X. Zhan *et al.*[32] reported on preparation of Sb_2Se_3-based microrobots of anisotropic crystal structure that were navigated under polarized light. Similarly, metal dichalcogenides, such as WS_2 and MoS_2, were

[a]*Center for Advanced Functional Nanorobots, Department of Inorganic Chemistry, University of Chemistry and Technology Prague, Technicka 5, 166 28 Prague, Czech Republic. E-mail: pumera.research@gmail.com*
[b]*Future Energy and Innovation Laboratory, Central European Institute of Technology, Brno University of Technology, Purkynova 656/123, 621 00, Brno, Czech Republic*
[c]*Faculty of Electrical Engineering and Computer Science, VSB – Technical University of Ostrava, 17. listopadu 2172/15, 70800 Ostrava, Czech Republic*
[d]*Department of Medical Research, China Medical University Hospital, China Medical University, No. 91 Hsueh-Shih Road, Taichung, Taiwan 40402*
† Electronic supplementary information (ESI) available. See DOI: https://doi.org/10.1039/d3nr00098b

applied for the fabrication of photophoretic swarming microrobots.[29,30]

Here, we fabricated swarming phoretic antimony(III) sulfide (Sb_2S_3)-based microrobots (further referred as "microrobots"). Sb_2S_3 is an earth-abundant semiconductor with low toxicity and good stability in air.[33] It shows remarkable optoelectrical properties suitable for solar cells[34] and lithium ion batteries fabrication,[35] photocatalytic water splitting[36] and photocatalytic pollutant degradation.[37,38] Being aware of current "green chemistry" trends,[39] our objective was to apply the synthetic approach to microrobots manufacturing in an environmentally friendly way. Therefore, we employed bio-originated precursors as capping agents, that is, proteogenic α-amino acid L-cysteine and tartaric acid, which occurs naturally in many types of fruits. The synthetic route was then carried out in a microwave reactor providing great reproducibility, low-energy usage, and large-scale production.[40,41] The resulting microrobots were propelled under ultraviolet (UV) light irradiation due to the electrophoretic and diffusiophoretic behavior of the microrobots. Since the electrophoretic and diffusiophoretic-induced propulsion is caused by ions and ROS formation and redistribution, we applied the microrobots for photocatalytical degradation of organic pollutants. As model pollutants, we chose tartrazine and quinoline yellow food dyes. Given their poor biodegradability, synthetic food dyes can accumulate in wastewater and negatively influence the environment.[42–44] Anionic azo-dye tartrazine (E 102) and anionic quinophthalone dye quinoline yellow (E 104) are claimed to induce allergic and intolerance reactions, particularly in asthmatics, and cause hyperactivity, especially in children.[45–47]

Results and discussion

Fabrication and characterization of microrobots

The Sb_2S_3 microrobots were prepared in a microwave reactor (Fig. 1) by reacting $SbCl_3$ (antimony(III) chloride) with biomaterial-based templates L-cysteine and tartaric acid. As suggested in a previous report,[48] Sb^{3+} forms a complex with tartaric acid and thus allows coupling *via* hydrogen bonds with L-cysteine, which acts as a sulfurizing agent to allow the formation of Sb_2S_3. To perform the synthesis in an environmentally friendly way, we proceeded the reaction in an aqueous environment. Although water is not considered the most efficient solvent to convert microwave irradiation into heat, especially in comparison to ethylene glycol, dimethyl sulfoxide, or methanol,[49] this synthetic approach showed great results and can be regarded as environmentally friendly.

To optimize the procedure, different reaction conditions were tested. Fig. S1† shows the influence of magnetic stirring, reaction time, temperature, and tartaric acid concentration on the resulting morphology of the microrobots. Briefly, stirring the reaction mixture during the synthesis enabled formation of homogeneous size and morphology distribution of microrobots. It is worth emphasizing that stirring is not typically allowed in conventional hydrothermal synthetic methods, but it can be applied and controlled in the case of using a microwave reactor. Next, the reaction time of 15 minutes caused the formation of spherical and rod-like microrobots together. After 30 minutes, only rod-shaped microrobots were obtained, suggesting homogeneous shape and size control. No further effect was observed when prolonging the reaction time to 45 minutes. The morphology was further influenced by the reaction temperature. The optimal temperature was evaluated at 180 °C as the lower temperature of 160 °C led to a reduction of microrobot size homogeneity; however, higher temperature of 200 °C caused only a slight increase in size homogeneity. Further, tartaric acid concentration was observed to have a significant effect on the resulting morphology of the microrobots as well. The optimal concentration of tartaric acid was evaluated as 8 mol. eq. with respect to $SbCl_3$. When the concentration was reduced to 6 mol. eq. with respect to $SbCl_3$, sponge-like microparticles were formed, whereas increasing the concentration to 10 mol. eq. with respect to $SbCl_3$ caused the formation of larger rods. The protocol of the optimized microwave-assisted synthetic procedure is shown in Fig. S2.† Namely, the temperature, pressure, and power profiles are presented. It is worth noting that the precise hold of the temperature during the synthesis enables high reproducibility of the material preparation. Moreover, the power of the microwave reactor is ~20 W after reaching the set temperature suggesting low-energy consumption mode during the synthesis.

After optimizing the synthetic procedure, the microrobots resembled rods with average length of 16 ± 5 μm and width of

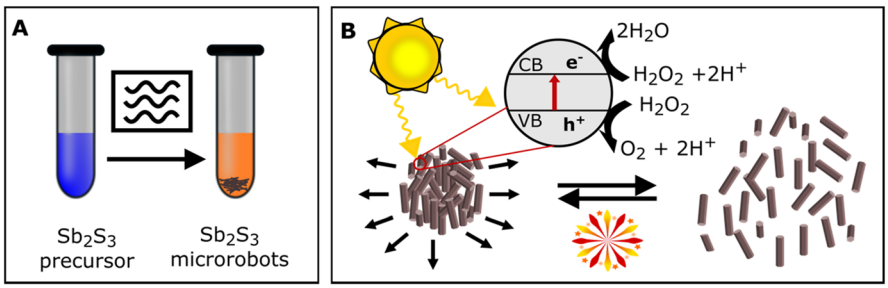

Fig. 1 Schematic illustration showing (A) the "one-pot" preparation of Sb_2S_3 microrobots using a microwave reactor and (B) their phoretic properties under light irradiation that induce swarming-like behavior. CB and VB stand for conduction and valence bands, respectively.

3.0 ± 0.9 μm (Fig. 2A). EDX images revealed a homogeneous presence of antimony and sulfur within the microrobots, suggesting that no antimony- or sulfur-rich domains were formed during the preparation (Fig. 2A). The EDX spectra are presented in Fig. S3.† The formation of the Sb_2S_3 phase was proved by recording Raman spectra. Fig. 2B demonstrates the well-resolved resulting Raman spectrum that points to the crystalline structure.[50] The peaks localized at 303, 282, and 254 cm^{-1} correspond to the Sb–S stretching vibration, and the peak at 190 cm^{-1} corresponds to the S–Sb–S bending vibration.[51] To confirm the crystalline nature of the microrobots, powder X-ray diffraction (powder XRD) analysis was performed. The resulting diffractograms (Fig. 2C) reveal a crystalline structure without signs of impurities. The diffractogram corresponded to the orthorhombic structure of stibnite with lattice parameters a = 11.33, b = 3.84, and c = 11.24 which is in agreement with reported data.[48] In the next step, we recorded absorption spectra of the powdered material to characterize its optical properties. As seen in Fig. 2D, the absorption occurs even in visible range, with the onset of absorption at around 750 nm. Assuming an indirect transition, the optical bandgap was estimated at 1.6 eV, which is in agreement with previous reports.[52]

It should be noted that during the typical hydrothermal preparation of Sb_2S_3 material, an amorphous phase is formed and further sintering is necessary to transform the material into a crystalline phase.[48,50] Based on the results discussed in the latter paragraph, the microwave irradiation obviously facilitated formation of the crystalline phase during the synthetic procedure. Therefore, the resulting material could be directly used for the desired application without any further energy-consuming and time-demanding thermal treatment. This observation is in agreement with previous findings in which microwave radiation assisted in the formation of high-quality crystalline structures.[53]

The microrobots were further characterized by measuring zeta potential in aqueous dispersions. The value of −40 ± 4 mV suggested the formation of stable colloidal solutions that do not require any further stabilization through the use of surfactants.

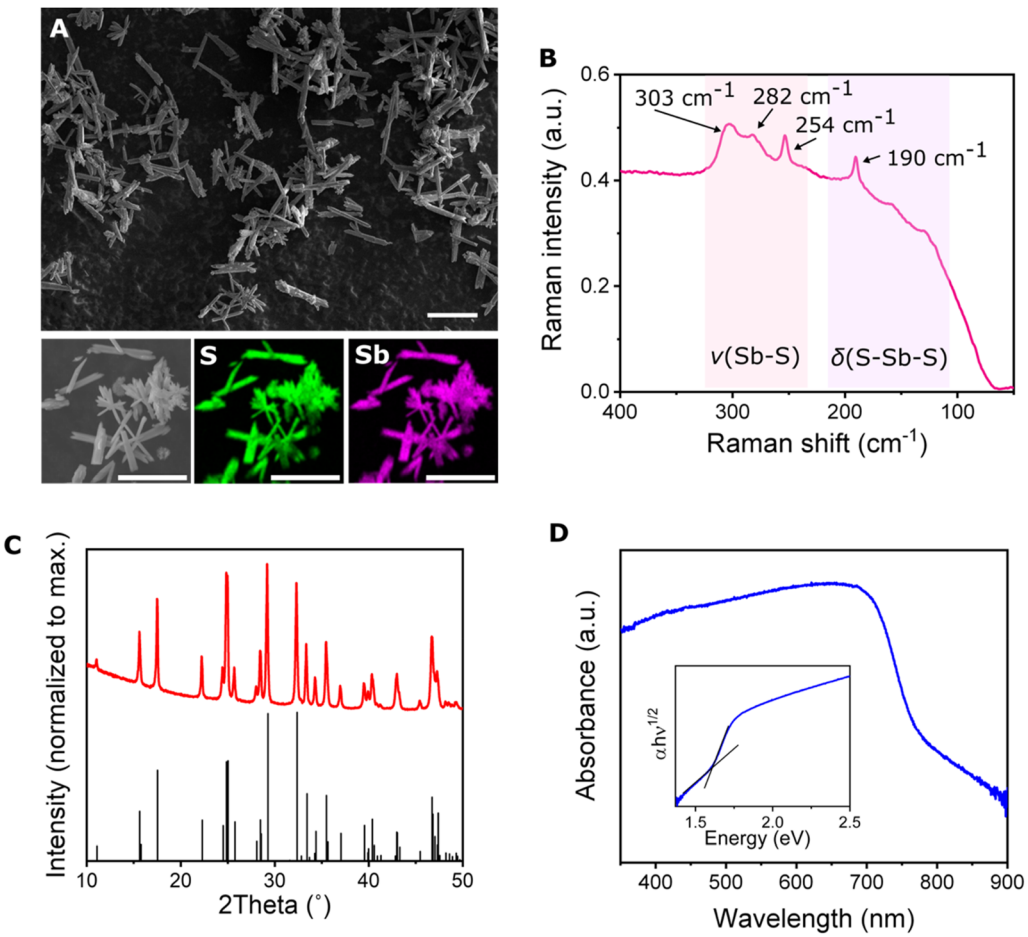

Fig. 2 Structural and optical characterization of microrobots. (A) SEM image of the microrobots and EDX elemental mapping images. Scale bar 25 μm. (B) Raman spectrum with labelled characteristic stretching (ν) and bending (δ) vibrations. (C) Powder XRD pattern of microrobots showing the characteristic fingerprint of the Sb_2S_3 material in comparison with the reference pattern (JCPDS No. 01-075-4015). (D) Absorption spectrum of microrobots with Tauc plot in the inset to determine optical bandgap.

Light-induced locomotion of microrobots

Initially, we tested whether the photocatalytic properties of Sb_2S_3 would enable self-propulsion of microrobots under UV light irradiation. As Fig. 3A and C demonstrate, moderate self-propulsion induced by UV irradiation was indeed observed (Video S1†). The average velocity of the microrobots under UV irradiation was 0.3 ± 0.1 μm s^{-1}. On the contrary, only Brownian motion was observed without any UV irradiation. To explain this observation, it should be noted that as a photoactive material, Sb_2S_3 is capable of light absorption; hence, suitable energy of irradiation can cause exciton formation where electrons (e^-) are accumulated in the conduction band and can interact on the surface of microrobots with protons generated from the interaction of holes (h^+) with water.[54] The process can be summarized by the following equations:

$$2H_2O + 4h^+ \rightarrow 4H^+ + O_2 \quad (1)$$

$$4H^+ + 4e^- \rightarrow 2H_2 \quad (2)$$

In addition to protons, oxygen, and hydrogen, different photogenerated species, such as O_2^-, $OH^\bullet$, and OH^-, can be formed by further interactions. Due to the non-symmetrical shape of microrobots, the ion gradient around an individual microrobot is not homogeneous, thus, self-electrophoretic motion is induced.[21,55]

To investigate the origin of the phenomenon deeper, we determined the photoelectrochemical properties of microrobots by plotting Tafel curves. As the Tafel curves (Fig. 3B) suggest, there is a significant shift of about 360 mV toward positive potential after exposure of the sample to UV irradiation. This observation supports our conclusions about photochemically driven locomotion.

Self-propulsion was further enhanced by applying hydrogen peroxide as a fuel (Video S2†). The photocatalytic decomposition of hydrogen peroxide forms reactive oxygen species (ROS) by the following equations:

$$H_2O_2 + 2h^+ \rightarrow 2H^+ + O_2 \quad (3)$$

$$H_2O_2 + 2e^- \rightarrow 2OH^- \quad (4)$$

Combining the interactions described in eqn (1)–(4), the concentration of ionic species and radicals increases, therefore the self-electrophoretic phenomenon is enhanced.[55]

The results of the velocity calculations are summarized in Fig. 3A. Obviously, the average velocity of the microrobots increased with increasing fuel concentration starting from the

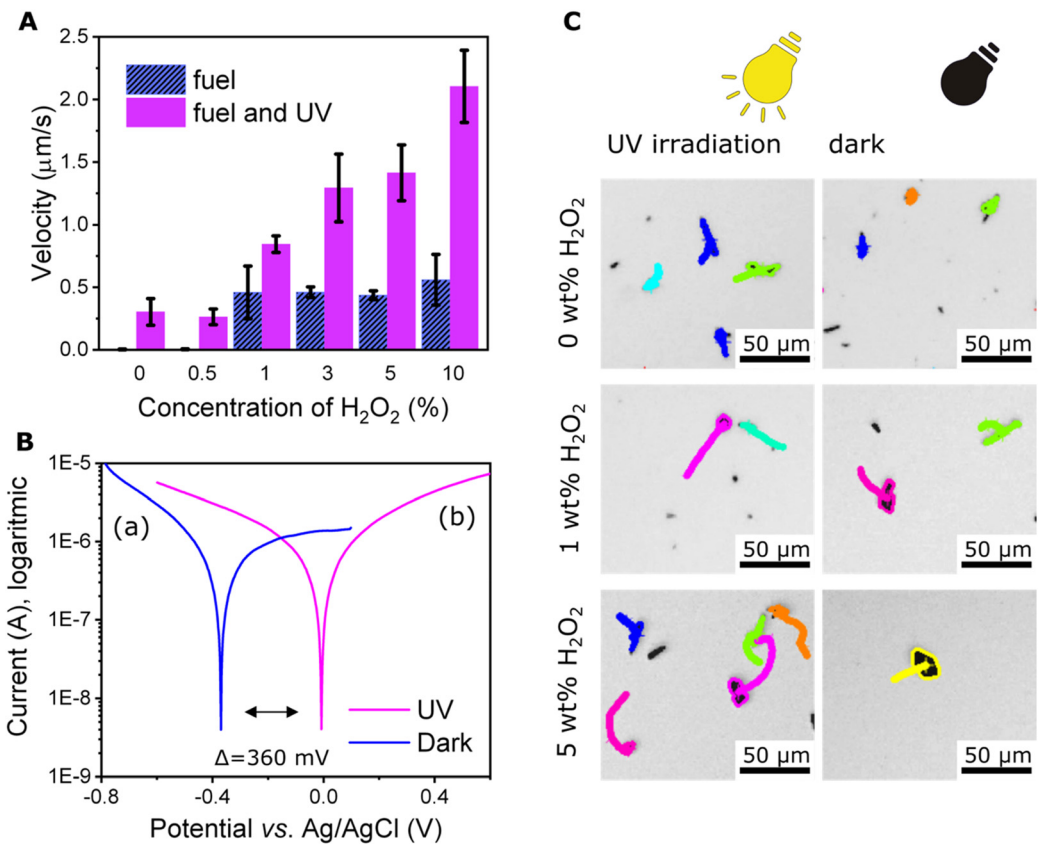

Fig. 3 Characterization of the locomotion of the microrobots. (A) Average velocity of microrobots at different fuel concentrations and the influence of UV irradiation. (B) Tafel plots of static microrobots to demonstrate photocatalytic activity. The Tafel curves were measured in pure water under dark conditions (a) and under UV irradiation (b). (C) Typical trajectories of microrobots at different conditions collected after 20 s.

concentration of 1 wt% hydrogen peroxide. Propulsion was also observed in the presence of >1 wt% hydrogen peroxide under dark conditions. However, in this case the average velocity did not depend on the concentration of hydrogen peroxide and remained constant in the range 0.4–0.5 μm s^{-1}.

Observing microrobots in their aqueous dispersion, a strong influence of UV irradiation on microrobots organization within the sample was observed. As Fig. 4 suggests, UV irradiation induces collective behavior and the swarms of microrobots expand (original micrographs without any labels are shown in Fig. S4†). Conversely, when UV light was switched off, the swarms started shrinking, suggesting a reversible process (Video S3†). Same phenomenon was previously observed in the case of titanium dioxide-based microrobots.[55] As mentioned above, Sb_2S_3 acts as a semiconductive photocatalyst and upon UV irradiation, ions and ROS are formed according to eqn (1)–(4). In addition to electrophoresis, other phenomena, such as osmotic propulsion and surface charge interaction, occur. Ions, radicals, and ROS are generated under UV irradiation, which leads to the accumulation of surface charge and electrostatic repulsions take place causing expansion of the swarms. Under dark conditions, the accumulated charged species induce electro-osmosis during their dissociation and diffusion, which obviously causes clustering of microrobots' swarms.[21,22,55] As expected, the addition of hydrogen peroxide increased the collective behavior due to more intensive ions and ROS generation. Comparison of light-induced swarming behavior of fueled and non-fueled microrobots is also demonstrated in Video S3.† To exclude photothermal related effects, such as thermal convection that is induced when the sample is locally heated with UV light,[28] non-photocatalytic polymer microparticles were studied at the same setting while applying 5% hydrogen peroxide as a fuel and irradiating the sample with UV light. As a result, no propulsion was induced in that experiment (Video S4†) suggesting that the swarming behavior of the microrobots was not caused by temperature gradients.

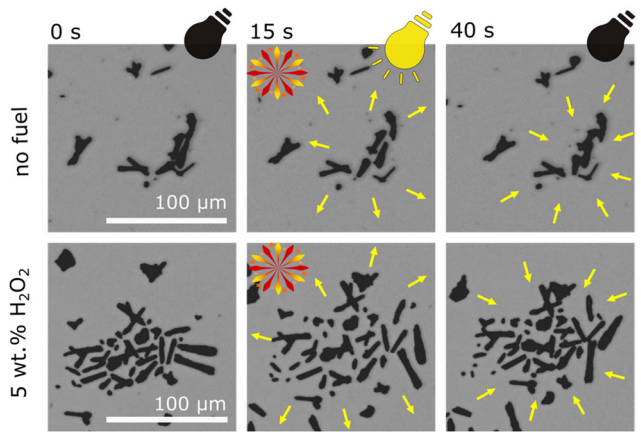

Fig. 4 Collective swarming behavior of microrobots as a function of UV irradiation. Comparison of fueled and non-fueled microrobots.

Photocatalytic degradation of food dyes

Taking into account the remarkable photocatalytic properties of Sb_2S_3, we employed microrobots for photocatalytic degradation of food dyes, *i.e.*, quinoline yellow and tartrazine. It was assumed that the active radicals, ions, and ROS produced under UV irradiation would be able to degrade the food dyes.

Quinoline yellow is an acid dye with a characteristic absorption spectrum due to the aromatic structure, with its maximum at 412 nm. On the other hand, tartrazine, as a member of azo-dye family, shows a characteristic absorption spectrum, with its maximum at 428 nm (Fig. S5†). In both cases, degradation is expected to cause a decrease in absorption bands due to the disruption of the structure.[56] Therefore, the degradation process was monitored by recording UV-Vis spectra of the samples. To perform the degradation experiments, stock solutions of food dyes were prepared and exposed to UV irradiation to first monitor stability without the presence of microrobots. After two hours of exposure to UV irradiation, the decrease in absorbance was ~7 and ~1% in the case of quinoline yellow and tartrazine, respectively, suggesting that both food dyes exhibit great stability when exposed to UV irradiation.

Prior the photocatalytic experiments, the samples containing microrobots alongside the food dyes were magnetically stirred for 20 minutes at dark conditions and the UV-Vis spectra were recorded to monitor the possible adsorption of dyes on the microrobots. However, no drop in the absorbance was detected during these equilibration experiments indicating that no adsorption occurred. In the next step, the samples were exposed to UV irradiation and the stability of food dyes was monitored using a spectrophotometer. Fig. 5 summarizes the degradation of food dyes as observed in the presence of microrobots. In the case of quinoline yellow, there was a 35% decrease in absorbance when microrobots were applied. In the case of tartrazine, the decrease in absorbance was by 17%, suggesting its better stability toward photocatalytic decomposition in this set up. The low degradation efficiency of tartrazine could be explained by different tendency toward photocatalytic degradation at different pH of solutions. In our study, no pH control was applied by using buffer solutions. The pH of the quinoline yellow and tartrazine solutions containing the microrobots were 6.5 and 6.4, respectively before the photocatalytic degradation experiments. As described in a previous study, photodegradation efficiency of tartrazine is higher at acidic conditions[57] whereas photodegradation of quinoline yellow showed to be the most efficient without any pH control.[58]

To investigate the degradation process of food dyes deeper, control experiments of the photodegradation of quinoline yellow were performed with ethylenediaminetetraacetic acid (EDTA). EDTA is a commonly used scavenger that interacts with photogenerated holes and hinders the formation of $OH^{\bullet}$ radicals.[59] As clearly demonstrated in Fig. S6,† the presence of the scavenger significantly decreased the efficiency of photo-

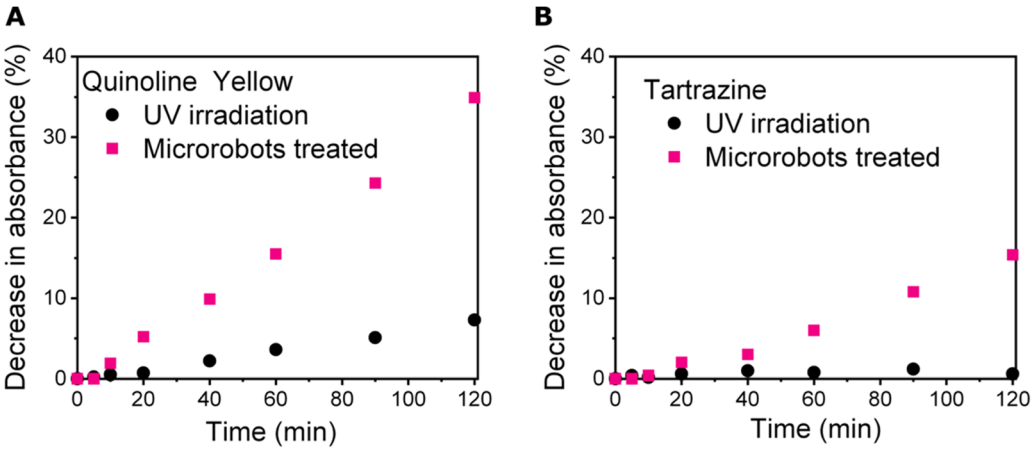

Fig. 5 Photodegradation of food dyes determined by the change in absorbance. Graphs show degradation of quinoline yellow (A) and tartrazine (B) using photocatalytically active microrobots and UV irradiation alongside the control experiment where no microrobots were applied.

catalytic degradation of quinoline yellow; the absorbance decreased by 22% after two hours This observation supports the assumption that the ROS, especially $OH^{\bullet}$ radicals are generated upon exposure of the microrobots under UV illumination providing the degradation abilities.

Conclusions

We employed a microwave-assisted technique to develop a reproducible, low-cost, and "green" manufacturing process of microrobots. It is worth noting that the original synthesis of the Sb_2S_3 material was performed in an autoclave at 180 °C for 12 hours and further annealing at 250 °C for 3 hours was necessary to obtain the crystalline structure.[48] Here, we performed the reaction in a microwave reactor at 180 °C for 30 min without any further thermal treatment. Sb_2S_3 was presented as photoactive material that enables the self-propulsion of the resulting microrobots under UV irradiation. Self-propulsion was further enhanced in the presence of hydrogen peroxide as a fuel. Due to their photocatalytic properties, microrobots were applied for the degradation of food dyes, namely, tartrazine and quinoline yellow. It can be expected that such microrobots can find application in the removal of residual food dyes and beyond.

Experimental

Materials

Antimony(III) chloride ($SbCl_3$, ≥99.5%), L-tartaric acid (≥99.5%), L-cysteine (97%), tartrazine (analytical standard), quinoline yellow (mixture of the mono- and disulfonic acids), ethylenediaminetetraacetic acid (EDTA, ≥98.5%), and hydrogen peroxide (30%) were obtained from Sigma Aldrich. Ethanol absolute A.G. was purchased from Penta. All chemicals were used as received.

Synthesis of Sb_2S_3 microrobots

For a typical microwave-assisted synthesis of Sb_2S_3 microrobots, $SbCl_3$ (0.46 mmol) was dissolved in 20 mL of tartaric acid stock solution (0.17 mol dm^{-3}) using a sonication bath. In the next step, L-cysteine (0.65 mmol) was added and the solution was magnetically stirred for 10 minutes. The precursor solution was transferred to a reaction vial and placed in the microwave reactor (Monowave 400, Anton Paar). The reaction was carried out at 180 °C for 30 minutes while being magnetically stirred (600 rpm). The crude product was collected by centrifugation (4000 rpm, 3 min) and washed with ultrapure water twice and with ethanol three times. The resulting microrobots were vacuum-dried at 40 °C overnight.

Characterization

Morphology was characterized using a MIRA 3 XMU (Tescan) scanning electron microscope equipped with an EDX detector (Oxford Instruments) for elemental mapping. Powder samples were characterized on an adhesive carbon tape.

Powder XRD characterization was performed using a Rigaku SmartLab 3 kW X-ray powder diffractometer with Cu Kα radiation source. Raman spectra were measured with an IR-Raman spectrometer (Bruker RFS 100) using a 9394.4 cm^{-1} laser for excitation. The absorption spectra of microrobots in solid state were recorded by a Jasco V-750 UV-Vis spectrometer equipped with an integrating sphere (ISV-922). The zeta potential was measured by Zetasizer Ultra (Malvern Panalytical Ltd) and an average of 5 measurements was calculated.

Tafel plots were obtained by performing linear sweep voltammetry on a PGSTAT 204 (Metrohm Autolab) equipped with UV LED (365 nm, 700 mA, radiant flux 3.3 W, LedEngin Inc.). For this purpose, microrobots' aqueous dispersion was drop-casted over an ITO substrate that was then dried at ambient conditions. Ag/AgCl and platinum electrodes were employed as reference and counter electrodes, respectively. The measurements were made in distilled water under dark conditions and under UV irradiation.

Locomotion analysis was performed using a Nicon Eclipse Ts2R inverted microscope equipped with a Basler ace acA1920-155uc digital camera. The microscope was also equipped with a UV-LED source (pE-100, 365 nm, 1670 W cm^{-2}). The sample for the locomotion analysis was prepared by placing a droplet of microrobots' solution (5 μl) on a glass slide. The concentration was adjusted according to the setting of microscope to obtain videos of at least 60 tracks. Alternatively, hydrogen peroxide was added to the microrobots in a specific amount to reach its desired concentration to act as fuel. The tracks of the microrobots were analyzed using the TrackMate plugin within ImageJ software.[60] A Python code subtracting eventual drift was used to calculate average velocities of each video.[61] The resulting velocities were obtained as an average and a standard deviation of at least three videos. Finally, the representative trajectories were visualized using NIS software.

Food dyes degradation experiments

The sample containing microrobots (0.2 mg mL^{-1}) and food dye (quinoline yellow or tartrazine, both 0.01 mg mL^{-1}) in total volume 20 mL was magnetically stirred for 20 min in a 50 mL reaction vial at dark conditions before the experiment. The sample was exposed to UV irradiation (365 nm, 700 mA, radiant flux 4.1 W, LedEngin Inc.) and aliquots were taken at given time intervals to monitor the degradation process. For this purpose, the sample was centrifuged (4000 rpm, 3 min) to remove microrobots and the absorption spectrum of the supernatant was recorded in quartz cuvettes (1 × 1 cm) using the UV-Vis spectrometer. The absorbance of quinoline yellow and tartrazine was read at 412 and 428 nm, respectively. The control experiment with EDTA was performed at same conditions with the modification that EDTA was added to the reaction mixture (0.1 mM) before the photocatalytic reaction.

Author contributions

A.J.P. performed the experiments, treated the data, and wrote the manuscript. M.P. supervised the project and revised the manuscript.

Conflicts of interest

There are no conflicts to declare.

Acknowledgements

This work was supported by the project Advanced Functional Nanorobots (reg. no. CZ.02.1.01/0.0/0.0/15_003/0000444 financed by the EFRR). CzechNanoLab project LM2018110 funded by MEYS CR is gratefully acknowledged for the financial support of the measurements at CEITEC Nano Research Infrastructure.

References

1 F. Soto, E. Karshalev, F. Zhang, B. Esteban Fernandez de Avila, A. Nourhani and J. Wang, Smart Materials for Microrobots, *Chem. Rev.*, 2022, **122**, 5365–5403.
2 B. Jurado-Sánchez and J. Wang, Micromotors for environmental applications: a review, *Environ. Sci.: Nano*, 2018, **5**, 1530–1544.
3 J. Li and M. Pumera, 3D printing of functional microrobots, *Chem. Soc. Rev.*, 2021, **50**, 2794.
4 J. V. Vaghasiya, C. C. Mayorga-Martinez, S. Matejkova and M. Pumera, Pick up and dispose of pollutants from water via temperature-responsive micellar copolymers on magnetite nanorobots, *Nat. Commun.*, 2022, **13**, 1026.
5 M. Urso, M. Ussia, F. Novotný and M. Pumera, Trapping and detecting nanoplastics by MXene-derived oxide microrobots, *Nat. Commun.*, 2022, **13**, 3573.
6 X. Peng, M. Urso, M. Ussia and M. Pumera, Shape-Controlled Self-Assembly of Light-Powered Microrobots into Ordered Microchains for Cells Transport and Water Remediation, *ACS Nano*, 2022, **16**, 7615–7625.
7 (*a*) M. Urso and M. Pumera, Nano/Microplastics Capture and Degradation by Autonomous Nano/Microrobots: A Perspective, *Adv. Funct. Mater.*, 2022, **32**, 2112120; (*b*) M. Urso, M. Ussia and M. Pumera, Smart micro- and nanorobots for water purification, *Nat. Rev. Bioeng.*, 2023, DOI: 10.1038/s44222-023-00025-9.
8 (*a*) H. Zhou, C. C. Mayorga-Martinez and M. Pumera, Microplastic Removal and Degradation by Mussel-Inspired Adhesive Magnetic/Enzymatic Microrobots, *Small Methods*, 2021, **5**, 2100230; (*b*) J. Kim, C. C. Mayorga-Martinez and M. Pumera, Magnetically boosted 1D photoactive microswarm for COVID-19 face mask disruption, *Nat. Commun.*, 2023, **14**, 935.
9 M. Ussia, M. Urso, S. Kment, T. Fialova, K. Klima, K. Dolezelikova and M. Pumera, Light-Propelled Nanorobots for Facial Titanium Implants Biofilms Removal, *Small*, 2022, **18**, 2200708.
10 M. Ussia, M. Urso, K. Dolezelikova, H. Michalkova, V. Adam and M. Pumera, Active Light-Powered Antibiofilm ZnO Micromotors with Chemically Programmable Properties, *Adv. Funct. Mater.*, 2021, **31**, 2101178.
11 J. Munoz, M. Palacios-Corella, I. J. Gómez, L. Zajíčková and M. Pumera, Synthetic Nanoarchitectonics of Functional Organic-Inorganic 2D Germanane Heterostructures via Click Chemistry, *Adv. Mater.*, 2022, **34**, 22067382.
12 C. C. Mayorga-Martinez, J. Vyskočil, F. Novotný, P. Bednar, D. Ruzek, O. Alduhaishe and M. Pumera, Collective Behavior of Magnetic Microrobots through Immuno-Sandwich Assay: On-The-Fly COVID-19 Sensing, *Appl. Mater. Today*, 2022, **16**, 101337.
13 B. Wang, K. Kostarelos, B. J. Nelson and L. Zhang, Trends in Micro-/Nanorobotics: Materials Development, Actuation, Localization, and System Integration for Biomedical Applications, *Adv. Mater.*, 2021, **33**, 2002047.

14 K. E. Peyer, L. Zhang and B. J. Nelson, Bio-Inspired Magnetic Swimming Microrobots for Biomedical Applications, *Nanoscale*, 2013, **5**, 1259–1272.
15 Y. Dong, L. Wang, K. Yuan, F. Ji, J. Gao, Z. Zhang, X. Du, Y. Tian, Q. Wang and L. Zhang, Magnetic Microswarm Composed of Porous Nanocatalysts for Targeted Elimination of Biofilm Occlusion, *ACS Nano*, 2021, **15**, 5056–5067.
16 C. C. Mayorga-Martinez, J. Zelenka, K. Klima, P. Mayorga-Burrezo, L. Hoan, T. Ruml and M. Pumera, Swarming Magnetic Photoactive Microrobots for Dental Implant Biofilm Eradication, *ACS Nano*, 2022, **16**, 8694–8703.
17 A. Jancik-Prochazkova, C. C. Mayorga-Martinez, J. Vyskočil and M. Pumera, Swarming Magnetically Navigated Indigo-Based Hydrophobic Microrobots for Oil Removal, *ACS Appl. Mater. Interfaces*, 2022, **14**, 45545–45552.
18 Q. Wang and L. Zhang, External Power-Driven Microrobotic Swarm: From Fundamental Understanding to Imaging-Guided Delivery, *ACS Nano*, 2021, **15**, 149–174.
19 J. Wang, Z. Xiong and J. Tang, The Encoding of Light-Driven Micro/Nanorobots: from Single to Swarming Systems, *Adv. Intell. Syst.*, 2021, **3**, 2000170.
20 J. Zhang, A. Laskar, J. Song, O. E. Shklyaev, F. Mou, J. Guan, A. C. Balazs and A. Sen, Light-Powered, Fuel-Free Oscillation, Migration, and Reversible Manipulation of Multiple Cargo Types by Micromotor Swarms, *ACS Nano*, 2022, DOI: **10.1021/acsnano.2c07266**.
21 B. Y. Hong, M. Diaz, U. M. Córdova-Figueroa and A. Sen, Light-Driven Titanium-Dioxide-Based Reversible Microfireworks and Micromotor/Micropump Systems, *Adv. Funct. Mater.*, 2020, **20**, 1568–1576.
22 J. Zhang, F. Mou, Z. Wu, J. Song, J. E. Kauffman, A. Sen and J. Guan, Cooperative transport by flocking phototactic micromotors, *Nanoscale Adv.*, 2021, **3**, 6157–6163.
23 L. Wang, A. Kaeppler, D. Fischer and J. Simmchen, Photocatalytic TiO_2 Micromotors for Removal of Microplastics and Suspended Matter, *ACS Appl. Mater. Interfaces*, 2019, **11**, 32937–32944.
24 Q. Zhang, R. Dong, X. Chang, B. Ren and Z. Tong, Spiropyran-Decorated SiO_2-Pt Janus Micromotor: Preparation and Light-Induced Dynamic Self-Assembly and Disassembly, *ACS Appl. Mater. Interfaces*, 2015, **7**, 24585–24591.
25 Y. S. Kochergin, K. Villa, F. Novotný, J. Plutnar, M. J. Bojdys and M. Pumera, Multifunctional Visible-Light Powered Micromotors Based on Semiconducting Sulfur- and Nitrogen-Containing Donor-Acceptor Polymer, *Adv. Funct. Mater.*, 2020, **30**, 2002701.
26 M. Ibele, T. E. Mallouk and A. Sen, Schooling Behavior of Light-Powered Autonomous Micromotors in Water, *Angew. Chem., Int. Ed.*, 2009, **48**, 3308–3312.
27 W. Duan, R. Liu and A. Sen, Transition between Collective Bahaviors of Micromotors in Response to Different Stimuli, *J. Am. Chem. Soc.*, 2013, **135**, 1280–1283.
28 Y. Hu, W. Liu and Y. Sun, Multiwavelength Phototactic Micromotor with Controllable Swarming Motion for "Chemistry-on-the-Fly", *ACS Appl. Mater. Interfaces*, 2020, **12**, 41495–41505.
29 M. Chen, Z. Lin, M. Xuan, X. Lin, M. Yang, L. Dai and Q. He, Programmable Dynamic Shapes with a Swarm of Light-Powered Colloidal Motors, *Angew. Chem., Int. Ed.*, 2021, **60**, 16674–16679.
30 V. De la Asunción-Nadal, D. Rojas, B. Jurado-Sánchez and A. Escarpa, Transition Metal Dichalcogenide Micromotors with Programmable Photophoretic Swarming Motion, *J. Mater. Chem. A*, 2022, DOI: **10.1039/D2TA07792B**.
31 R. Woods-Robinson, Y. Han, H. Zhang, T. Ablekim, I. Khan, K. A. Persson and A. Zakutayev, Wide Band Gap Chalcogenide Semiconductors, *Chem. Rev.*, 2020, **120**, 4007–4055.
32 X. Zhan, J. Zhen, Y. Zhao, B. Zhu, R. Cheng, J. Wang, J. Liu, J. Tang and J. Tang, From Strong Dichroic Nanomotor to Polarotactic Microswimmer, *Adv. Mater.*, 2019, **31**, 1903329.
33 H. Lei, J. Chen, Z. Tan and G. Fang, Review of Recent Progress in Antimony Chalcogenide-Based Solar Cells: Materials and Devices, *Sol. RRL*, 2019, 1900026.
34 R. Kondrotas, C. Chen and J. Tang, Sb_2S_3 Solar Cells, *Joule*, 2018, **2**, 857–878.
35 X. Zhou, L. Bai, J. Yan, S. He and Z. Lei, Solvothermal synthesis of Sb_2S_3/C composite nanorods with excellent Li-storage performance, *Electrochim. Acta*, 2013, **108**, 17–21.
36 A. D. DeAngelis, K. C. Kemp, N. Gaillard and K. S. Kim, Antimony(III) Sulfide Thin Films as a Photoanode Material in Photocatalytic Water Splitting, *ACS Appl. Mater. Interfaces*, 2016, **8**, 8445–8451.
37 J. Zhou, J. Chen, M. Tang, Y. Liu, X. Liu and H. Wang, Facile synthesis of an urchin-like Sb_2S_3 nanostructure with high photocatalytic activity, *RSC Adv.*, 2018, **8**, 18451.
38 L. Dashairya, M. Sharma, S. Basu and P. Saha, Enhanced dye degradation using hydrothermally synthesized nano-structured Sb_2S_3/rGO under visible light irradiation, *J. Alloys Compd.*, 2018, **735**, 234–245.
39 J. B. Zimmerman, P. T. Anastas, H. C. Erythropel and W. Leitner, Designing for a green chemistry future, *Science*, 2020, **367**, 397–400.
40 C. O. Kappe, Microwave dielectric heating in synthetic organic chemistry, *Chem. Soc. Rev.*, 2008, **37**, 1127–1139.
41 I. Bilecka and M. Niederberger, Microwave chemistry for inorganic nanomaterials synthesis, *Nanoscale*, 2010, **2**(8), 1358–1374.
42 S. Friorito, F. Epifano, L. Palumbo, C. Collevecchio, M. Bastianini, F. Cardellini, R. Spogli and S. Genovese, Efficient removal of tartrazine from aqueous solutions by solid sorbents, *Sep. Purif. Technol.*, 2022, **290**, 120910.
43 F. G. Nejad, I. Sheikshoaie and H. Beitollahi, Simultaneous detection of carmoisine and tartrazine in food samples using GO-Fe_3O_4-PAMAM and ionic liquid based electrochemical sensor, *Food Chem. Toxicol.*, 2022, **162**, 112864.
44 J. M. Navia-Mendoza, O. A. E. Filho, L. A. Zambrano-Intriago, N. R. Maddela, M. M. M. B. Duarte, L. S. Quiroz-Fernández, R. J. Baquerizo-Crespo and J. M. Rodríguez-

Díaz, Advances in the Application of Nanocatalysts in Photocatalytic Processes for the Treatment of Food Dyes: A Review, *Sustainability*, 2021, **13**, 11676.

45 P. Amchova, H. Kotolova and J. Ruda-Kucerova, Health safety issues of synthetic food colorants, *Regul. Toxicol. Pharmacol.*, 2015, **73**, 914–922.

46 Scientific Opinion of the Panel of Food Additives, Flavourings, Processing Aids and Food Contact Materials (AFC) on a request from the Comission on the results of the study by Mc Cann, *et al.*, 2007 on the effect of some colours and sodium benzoate on children's behavior. *EFSA J.*, 2008, **660**, 3–54.

47 S. I. Kaya, A. Cetinkaya and S. A. Ozkan, Latest advances on the nanomaterials-based electrochemical analysis of azo toxic dyes Sunset Yellow and Tartrazine in food samples, *Food Chem. Toxicol.*, 2021, **156**, 112524.

48 J. Pan, S. Xiong, B. Xi, J. Li, J. Li, H. Zhou and Y. Qian, Tartaric Acid and L-Cysteine Synergistic-Assisted Synthesis of Antimony Trisulfide Hierarchical Structures in Aqueous Solution, *Eur. J. Inorg. Chem.*, 2009, 5302–5306.

49 J. M. Kremsner and A. Stadler, *A Chemist's Guide to Microwave Synthesis. Basics, Equipment & Application Examples*, Anton Paar GmbH, 2018.

50 C. L. Hassam, F. Sciortino, N. T. K. Nguyen, B. Srinivasan, K. Ariga, F. Gascoin, F. Grasset, T. Mori, T. Uchikoshi, Y. Thimont and D. R. Berthebaud, Transparent Hybrid Thin Films of Phase-Change Material Sb_2S_3 Prepared by Electrophoretic Deposition, *ACS Appl. Energy Mater.*, 2021, **4**, 9891–9901.

51 B. Minceva-Sukarova, G. Jovanovski, P. Makreski, B. Soptrajanov, W. Griffith, R. Willis and I. Grzetic, Vibrational spectra of $M^IM^{III}S_2$ type synthetic minerals (M^I=Tl or Ag and M^{III}=As or Sb), *J. Mol. Struct.*, 2003, **651–653**, 181–189.

52 Z. Cui, K. Bu, Y. Zhuang, M. E. Donnelly, D. Zhang, P. Dalladay-Simpson, R. T. Howie, J. Zhang, X. Lü and Q. Hu, Phase transition mechanism and bandgap engineering of Sb_2S_3 at gigapascal pressures, *Commun. Chem.*, 2021, **4**, 125.

53 J. Jancik, A. Jancik Prochazkova, M. C. Scharber, A. Kovalenko, J. Masilko, N. S. Sariciftci, M. Weiter and J. Krajcovic, Microwave-Assisted Preparation of Organo-Lead Halide Perovskite Single Crystals, *Cryst. Growth Des.*, 2020, **20**, 1388–1393.

54 P. Myagmarsereejid, M. Ingram, M. Batmunkh and Y. L. Zhond, Doping Strategies in Sb_2S_3 Thin Films for Solar Cells, *Small*, 2021, **17**, 2100241.

55 P. Xu, S. Duan, Z. Xiao, Z. Yang and W. Wang, Light-powered active colloids from monodisperse and higly tunable microspheres with a thin TiO_2 shell, *Soft Matter*, 2020, **16**, 6082–6090.

56 P. Oancea and V. Meltzer, Photo-Fenton process for the degradation of Tartrazine (E102) in aqueous medium, *J. Taiwan Inst. Chem. Eng.*, 2013, **44**, 990–994.

57 Y. Zhou, Y. Qin, W. Dai and X. Luo, Highly Efficient Degradation of Tartrazine with a Benzoic Acid/TiO_2 System, *ACS Omega*, 2019, **4**, 546–554.

58 A. Tab, M. Dahmane, B. Chemseddin, B. Bellal, M. Trari and C. Richard, Photocatalytic Degradation of Quinoline Yellow over Ag_3PO_4, *Catalysts*, 2020, **10**, 1461.

59 X. Peng, M. Urso, J. Balvan, M. Masarik and M. Pumera, Self-Propelled Magnetic Dendrite-Shaped Microrobots for Photodynamic Prostate Cancer Therapy, *Angew. Chem., Int. Ed.*, 2022, **61**, e202213505.

60 D. Ershov, M.-S. Phan, J. W. Pylvänäinen, S. U. Rigaud, L. Le Blanc, A. Charles-Orszag, J. R. W. Conway, R. F. Laine, N. H. Roy, D. Bonazzi, G. Dumenil, G. Jacquemet and J.-Y. Tinevez, Bringing TrackMate in the era of machine-learning and deep-learning, *BioRxiv*, 2021. DOI: **10.1101/2021.09.03.458852**.

61 D. B. Allan, T. Caswell, N. C. Keim, C. M. van der Wel and R. W. Verweij, *Soft-matter/trackpy: Trackpy v0.5.0 (Version v0.5.0)*. Zenodo, 2021. **https://zenodo.org/record/4682814#.Yimwfi8w1QI**.